Journal of Materials Chemistry A

ROYAL SOCIETY OF CHEMISTRY

PAPER

View Article Online
View Journal

Cite this: DOI: 10.1039/d5ta08870d

Demonstrating electrochemical CO_2 capture on redox-active metal–organic frameworks

Iuliia Vetik, [a] Nikita Žoglo, [b] Akmal Kosimov, [c] Ritums Cepitis, [c] Veera Krasnenko, [d] Jaan Leis, [a] Maike Käärik, [a] Artis Kons, [e] Huilin Qing, [f] Priyanshu Chandra, [f] Katherine A. Mirica, [f] Ruben Rizo, [c] Enrique Herrero, [c] Jose Solla-Gullón, [c] Teedhat Trisukhon, [g] Jamie W. Gittins, [g] Alexander C. Forse, [g] Vitali Grozovski, [a] Nadezda Kongi *[a] and Vladislav Ivaništšev *[e]

Addressing climate change calls for action to control CO_2 pollution. Direct air capture offers a solution to this challenge. Making carbon capture competitive with alternatives, such as forestation and mineralisation, requires fundamentally novel approaches and ideas. One such approach is electrosorption, which is currently limited by the availability of suitable electrosorbents. In this work, we introduce a copper-2,3,6,7,10,11-hexahydroxytriphenylene ($Cu_3(HHTP)_2$) metal–organic framework (MOF) that can act as an electrosorbent for CO_2 capture, thereby expanding the palette of materials that can be used for this process. $Cu_3(HHTP)_2$ is the first MOF to switch its ability to capture and release CO_2 in aqueous electrolytes. By using cyclic voltammetry (CV), electrochemical impedance spectroscopy (EIS), galvanostatic charge–discharge (GCD) analysis, and differential electrochemical mass spectrometry (DEMS), we demonstrate reversible CO_2 electrosorption. Based on density functional theory (DFT) calculations, we provide atomistic insights into the mechanism of electrosorption and conclude that efficient CO_2 capture is facilitated by a combination of redox-active copper atoms and aromatic HHTP ligands within $Cu_3(HHTP)_2$. By showcasing the applicability of $Cu_3(HHTP)_2$ – with a CO_2 capacity of 2 mmol g^{-1} and an adsorption enthalpy of −20 kJ mol^{-1}, this study encourages further exploration of conductive redox-active MOFs in the search for superior CO_2 electrosorbents.

Received 31st October 2025
Accepted 27th April 2026

DOI: 10.1039/d5ta08870d

rsc.li/materials-a

Introduction

As a result of human activity, numerous environmental problems have been created. Global warming driven by CO_2 emissions constitutes the most pressing problem. This escalating issue poses severe threats to sustainability, making it a critical challenge to not only capture atmospheric CO_2 but also to make use of it.[1–4] Direct air capture is central for reducing atmospheric CO_2 concentration to target pre-industrial levels.[5–10] In carbon capture, there are two typically utilised methods – absorption and adsorption.[11] On one hand, absorption involves the dissolution of CO_2 into the bulk medium through chemical reactions, such as those with polyamines, or through strong physical interactions, for example, in ionic liquids.[12,13] Conversely, adsorption relies on weak physical attraction for CO_2 to adhere to a surface, such as in zeolites.[14,15] Recently, electrosorption has emerged as a promising alternative, combining strong chemisorption at specific applied potentials and weak physisorption at open circuit potentials.[16–23] This approach has enabled the development of high-performance CO_2 capture materials, such as polyanthraquinone (AQ).

In Fig. 1, we summarise previous progress in CO_2 sorbents comparing their capture capacity and sorption–desorption energy. As seen from the graph, AQ lies at the Pareto forefront with high sorption energy and capacity, similarly to polyamines. Ionic liquids and zeolites lie at the lower edge of the same front with low sorption energy and capacity. The green region above the Pareto forefront is the global target, which corresponds to the best trade-off between the capacity and energy expenditure.[35]

Electrosorption-based CO_2 capture represents an economically viable approach to combating the issue of global warming – a recent assessment finds electrochemical technologies to outperform others in all scenarios, especially when powered

[a]Institute of Chemistry, University of Tartu, Tartu 50411, Estonia. E-mail: nadezda.kongi@ut.ee
[b]RedoxNRG OÜ, Narva-Jõesuu 29021, Estonia
[c]Institute of Electrochemistry, University of Alicante, Apdo. 99, 03080, Alicante, Spain
[d]Institute of Physics, University of Tartu, Tartu 50411, Estonia
[e]Department of Chemistry, University of Latvia, Riga LV-1004, Latvia
[f]Department of Chemistry, Burke Laboratory, Dartmouth College, New Hampshire 03755, USA
[g]Yusuf Hamied Department of Chemistry, University of Cambridge, Cambridge CB2 1EW, UK

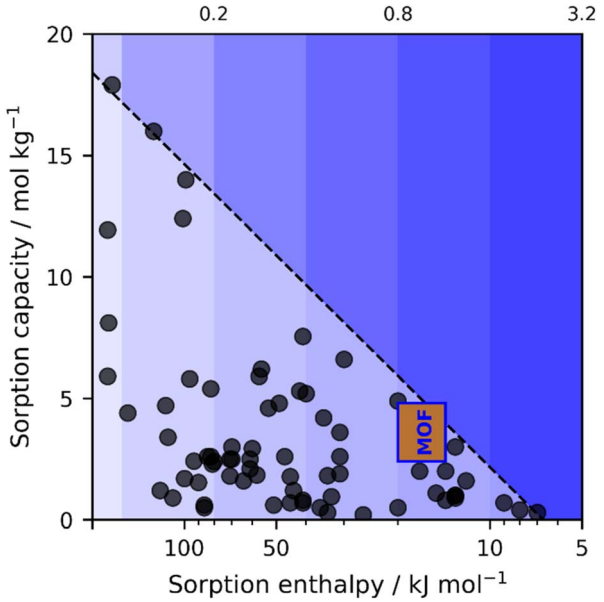

Fig. 1 Diagram of state-of-the-art CO_2 sorbents in terms of sorption capacity and energy. Calcium oxide, polyanthraquinone, various ionic liquids, and $Cu_3(HHTP)_2$ (MOF, rectangle) form a Pareto front (dashed line).[24–34] At the same time, other capture–release materials fall behind. All data are from ref. 25. $Cu_3(HHTP)_2$ is characterised by an adsorption energy of 14–20 kJ mol^{-1}, as obtained through DFT modelling and CV measurements, and CO_2 capacities of 2.4–4.8 mmol g^{-1}, as estimated from CV measurements under the assumption that the transfer of 0.5–1 electrons induces adsorption of one CO_2 molecule. The blue gradient represents electricity price (given above the plot in $ per kWh) at which the cost for capture–release is still below the targeted 100 $ per ton of CO_2. Favorable materials lie toward the upper right, *i.e.* combining high capacity with low regeneration cost.

with renewable electricity.[23] However, due to the novelty of the field, the range of known materials is limited and state-of-the-art electrosorbents have mainly been studied in non-aqueous solutions and inert atmospheres.[36–38] Moreover, in known materials, the electrosorption mechanism typically involves a single variable – a specific redox-active centre – inherently restricting the chemical space of suitable compositions.[39–42]

In this context, metal-2,3,6,7,10,11-hexahydroxytriphenylene (metal-HHTP) metal–organic frameworks (MOFs) are increasingly recognised for their electrochemical applications, including batteries, supercapacitors, and sensors,[43–48] since they combine redox properties of metals and aromaticity of HHTP (Fig. 2a). Having two variables in redox-active MOFs – metals and ligands – squares the corresponding chemical space of possible compositions, greatly expanding the scope of applicable materials. Metal-HHTP MOFs are characterised by crystalline structure, nanoscale porosity, and extensive surface area.[49,50] Moreover, the conjugated electronic structure of the HHTP ligand facilitates both in-plane π–d interactions and out-of-plane π–π stacking, resulting in high electrical conductivity.[49–52] Such a combination of straight diffusion pathways, high electron mobility, and dense redox-active sites in conductive MOFs makes them a promising new class of tunable porous materials for CO_2 electrosorption. Namely, assuming that all oxygen (O) atoms within metal-HHTP MOFs are capable of CO_2 electrosorption – capacities up to 14.5 mmol of CO_2 per g of MOF can hypothetically be achieved. Thus, we have chosen to explore Co-, Ni-, and Cu-HHTP MOFs and found that among these, $Cu_3(HHTP)_2$ exhibits a capacity comparable to those of long-known and optimised sorbents (Fig. 1 and Table S1).

In this article, we introduce $Cu_3(HHTP)_2$ as the first redox-active MOF that electrosorbs CO_2 from an aqueous solution at ambient temperature. Using cyclic voltammetry (CV), electrochemical impedance spectroscopy (EIS), galvanostatic charge–discharge (GCD) tests, and differential electrochemical mass spectrometry (DEMS), we demonstrate the suitability of $Cu_3(HHTP)_2$ for reversible CO_2 electrosorption. Using density functional theory (DFT) modelling, we provide atomistic insights into the electrosorption mechanism, revealing how the combination of redox properties of Cu and the aromatic system enables CO_2 chemisorption. Most importantly, this study demonstrates the key parameters that, when optimised, could lead to scalable and energy-efficient solutions for tackling global warming driven by CO_2 emissions.

Results and discussion

Structural characterisation

Since its initial synthesis in the 2010s, various $Cu_3(HHTP)_2$ morphologies, such as rod-, block- and agglomerated flake-like particles, have been reported.[53,54] Among these, the latter shows the best electrochemical performance in terms of capacitance.[53] Therefore, we synthesised the aforementioned flake-like morphology of $Cu_3(HHTP)_2$ (Fig. 2a), which was confirmed by scanning electron microscopy (SEM) analysis (Fig. 2b), elemental analysis, and specific surface area measurements (Fig. S1, S2, Tables S2 and S3). Simulated and measured powder X-ray diffraction (PXRD) confirms the crystallinity of the material (Fig. 2c). The Pawley refinement showed that the MOF sample contains only one phase, corresponding to the stacked $Cu_3(HHTP)_2$ (Fig. S3). The synthesised $Cu_3(HHTP)_2$ appears as a layered material with hexagonal pores and slipped-parallel layer stacking (Fig. 2d and e).[55,56] Each Cu atom coordinates with four O atoms in the plane. The slipped-parallel layered stacking allows two-thirds of Cu atoms to coordinate with two additional O atoms from adjacent layers (as shown in Fig. 2e and f).[53,56,57]

Although model structures of MOFs are available,[58] specifically modelling porous systems under electrochemical conditions is technically challenging due to methodological limitations and the high computational cost of accounting for pore geometry. Combining density functional theory (DFT) calculations with molecular dynamics allows the study of physisorption processes,[59] alas, at a high cost. Thus, only a limited number of systems can be modelled. Incorporating CO_2 into such hybrid simulations complicates calculations even further. Hence, for this study, we have developed two-dimensional models of $Cu_3(HHTP)_2$ pores (Fig. S4 and 2f) and run DFT calculations of electrochemical processes under constant potential and charge conditions.[60] Fig. 2f shows that in this model, CO_2 chemisorbs exclusively at the O sites of the MOF upon application of the potential.

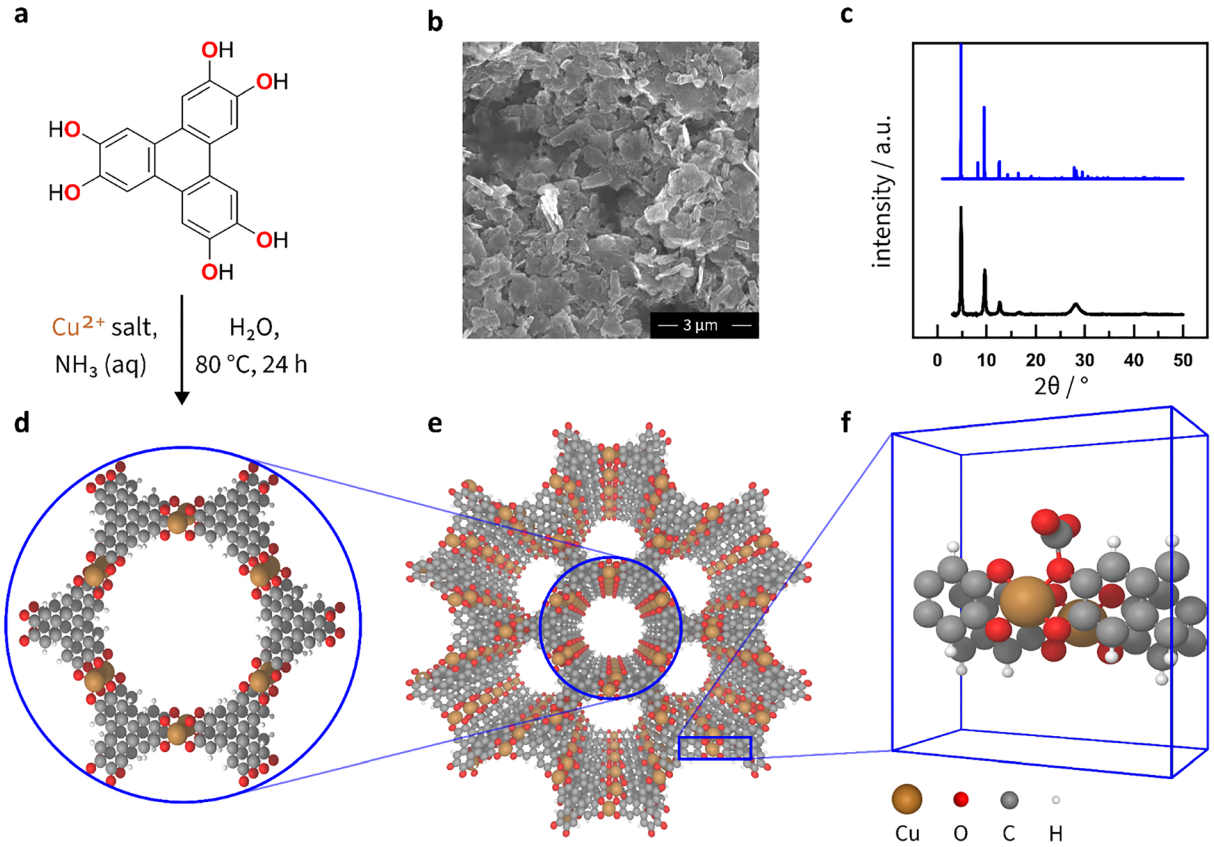

Fig. 2 (a) Scheme for the hydrothermal synthesis of $Cu_3(HHTP)_2$, (b) SEM image of $Cu_3(HHTP)_2$, (c) simulated (blue) and experimental (black) PXRD patterns for $Cu_3(HHTP)_2$. (d) Schematic representation of the hexagonal structure of the $Cu_3(HHTP)_2$, (e) top view of the $Cu_3(HHTP)_2$ structure with a slipped-parallel stacking mode. (f) A simplified model used for DFT-based simulations of CO_2 adsorption. Grey spheres represent C, red – O, ochre – Cu, and white – H atoms.

Fig. 2e and f illustrate that, as a result of slipped-parallel layer stacking and small O–O distance, only a fraction of O atoms are accessible for CO_2 chemisorption. In this case, all Cu atoms are completely sterically enclosed within the pore. Although some Cu and O atoms at the terminal surfaces of $Cu_3(HHTP)_2$ microcrystals should be open for adsorption, this out-pore surface area is negligible compared to the in-pore surface area, even for the flake-like morphology.

Electrochemical characterisation

Cyclic voltammetry measurements demonstrated the capacitive behaviour of $Cu_3(HHTP)_2$ after stabilisation by cycling for 2 hours in an Ar-saturated electrolyte (black curve in Fig. 3a and S5). Such behaviour is similar to the capacitive charging of thin layers and fine agglomerates of $Cu_3(HHTP)_2$,[61,62] as discussed in Fig. S5.

In a CO_2-saturated solution, CV measurements showed a reversible redox process (red and blue lines in Fig. 3a) corresponding to CO_2 adsorption and desorption. According to the CV curves in Fig. 3a, electrosorption on $Cu_3(HHTP)_2$ conceptually differs from electrosorption on anthraquinones.[63–65] For the latter, peaks in CV indicate reduction–oxidation of specific groups (with and without CO_2), which upon reduction can adsorb CO_2. In the absence of CO_2, $Cu_3(HHTP)_2$ shows no peaks, meaning that upon charging, electrons are distributed within the material (see the black curve in Fig. 3a), yet at a potential below +0.2 V, an electron transfer couples with CO_2 adsorption (see red curve in Fig. 3a).

To establish proof-of-concept electrosorption performance in aqueous media, we evaluated long-term cycling stability, energy efficiency, and the direct detection of CO_2 capture/release under simulated direct air capture conditions. Energy consumption and resistance characteristics were measured to further evaluate the electrochemical performance of $Cu_3(HHTP)_2$ in CO_2 capture/release. Galvanostatic charge–discharge (GCD) measurements were performed to quantify the energy requirements of the adsorption–desorption process (Fig. S6). The mean charge energy, determined by integrating the charge–discharge curves, was 8.5×10^{-9} Wh, while the discharge energy was 7.2×10^{-9} Wh, corresponding to an overall energy efficiency of 85%. In addition, interpretation of the electrochemical impedance spectroscopy (EIS) data showed that the process is limited by mass transport, *i.e.*, diffusion of ions through pores, rather than electron transfer (Fig. S7 and Table S4).

To distinguish between CO_2 adsorption and pH-induced carbonate-related effects, we measured CV curves in $NaHCO_3$ and Na_2CO_3 electrolytes in the absence of CO_2 flow. This

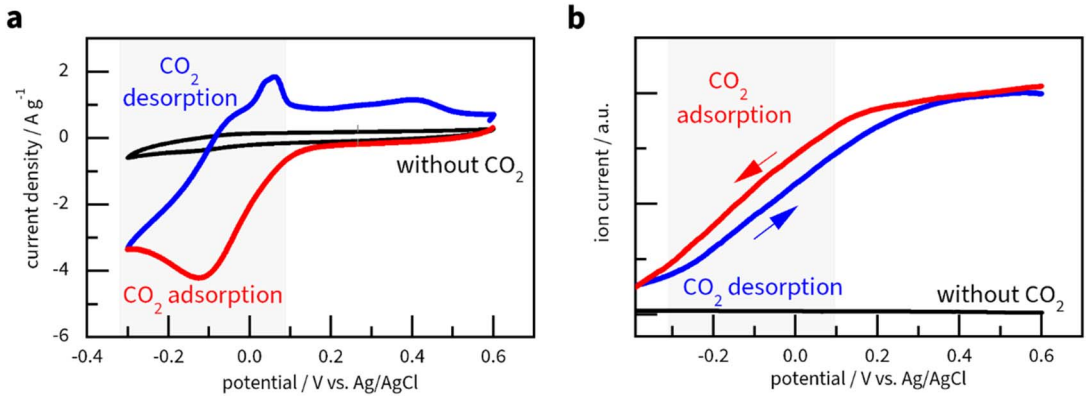

Fig. 3 (a) CV curves recorded at $v = 10$ mV s^{-1} for the $Cu_3(HHTP)_2$-modified GC electrode: black line – in an Ar-saturated electrolyte after stabilisation by cycling for two hours (without CO_2), red line – scan in the negative direction in a CO_2-saturated electrolyte, blue line – scan in the positive direction in a CO_2-saturated electrolyte. (b) DEMS ion current for $m/z = +44$ $[CO_2]^+$ during CV at $v = 1$ mV s^{-1} for the $Cu_3(HHTP)_2$-modified GC electrode: red line – scan in the negative direction in a CO_2-saturated electrolyte (showing adsorption from +0.2 V to −0.4 V); blue line – scan in the positive direction in a CO_2-saturated electrolyte (showing CO_2 desorption from −0.3 V to +0.5 V); black line – in an Ar-saturated electrolyte (without CO_2).

resulted in a noticeable decrease in current density (Fig. S8), suggesting that carbonate and bicarbonate ions do not induce the characteristic redox behaviour observed under CO_2-saturated conditions. In contrast, when gaseous CO_2 was introduced, the current density increased, and redox peaks appeared, identical to those observed in Fig. 3a. These results confirm that the electrochemical response is caused primarily by the adsorption of gaseous CO_2 rather than carbonate species formed through CO_2 hydrolysis. Therefore, while pH controls carbon speciation in general DAC contexts, the intrinsic molecular selectivity of the $Cu_3(HHTP)_2$ material ensures that the sorption process is insensitive to bicarbonate or carbonate presence.

To qualitatively confirm CO_2 adsorption–desorption, we applied differential electrochemical mass spectrometry (DEMS) – a technique for monitoring gas adsorption and desorption processes by detecting molecular ion signals in real-time.[66] In this study, DEMS was used to monitor the $[CO_2]^+$ ion current at $m/z = +44$ (ref. 67 and 68) during a CV sweep from −0.4 V to +0.6 V (Fig. 3b and S9). It should be stressed that DEMS shows cumulative changes in CO_2 sorption by the MOF, which, instead of reproducing discrete peaks, shows either a plateau (no sorption) or a slope (active adsorption or desorption). Moreover, the sweep rate is lower (1 mV s^{-1}) than that used in the CV measurements (10 mV s^{-1}) due to the time resolution of DEMS.[69] Most importantly, control experiments without CO_2 flow showed no CO_2 signals, confirming that DEMS specifically detects adsorbed and desorbed CO_2 (Fig. 3b). During the cathodic scan (red line), the CO_2 signal remained relatively stable between +0.6 V and +0.2 V, indicating that $Cu_3(HHTP)_2$ does not adsorb CO_2 within this potential range. A rapid, linear decrease in detected CO_2 occurred from +0.1 V to −0.3 V, which implies the adsorption of CO_2 by the MOF. Active desorption occurred between −0.3 V and +0.5 V (blue line), in accordance with the CV in Fig. 3a. The agreement between CV and DEMS results suggests reversible CO_2 electrosorption on $Cu_3(HHTP)_2$ to happen most actively between −0.3 and +0.3 V *vs.* Ag/AgCl.

CO_2 adsorption in a charged MOF is a slow process. Thus, to reach the maximum CO_2 capacity of $Cu_3(HHTP)$, we swept the potential from +0.6 V to −0.3 V and held it for a variable amount of polarisation time. Ten minutes were enough to saturate the MOF with CO_2 (Fig. 4a), *i.e.*, to reach a constant CO_2 capacity value. The CV curve shows one cathodic (C1) and multiple (A1–A4) anodic peaks with a separation of 150 mV between C1 and A1 peaks. If the process were purely thermodynamic, this separation would be directly related to the free energy of adsorption and desorption of around 14 kJ mol^{-1}. The amplitude of the peaks depends on the experimental conditions, like electrolyte composition, polarisation time, and sweep rate – very similar to anthraquinones.[39] From repeated experiments, we identified four anodic peaks at +0.05 V (A1), +0.13 V (A2), +0.27 V (A3) and +0.42 V (A4). Notably, the area under these peaks remains roughly the same in measurements run after keeping the MOF in Ar-saturated (Fig. 4a), O_2-saturated (Fig. 4b), and air-saturated (Fig. S10) electrolytes, which indicates the stability of $Cu_3(HHTP)_2$ under conditions close to ambient. Assuming that the current is linked to CO_2 desorption as one electron per one CO_2 molecule, we report a capacity of 2 mmol of CO_2 per gram of $Cu_3(HHTP)_2$. One electron is needed to reduce Cu^{2+}, whereas adsorption happens on O sites surrounding the reduced Cu^+. This suggests a possibility for the adsorption of more than one CO_2 molecule per electron.

Accordingly, we attribute the multiple anodic peaks (A1–A4) to the coupled oxidation–desorption process. As suggested by previous studies,[39,40] the neighbouring adsorbed CO_2 molecules repel each other. Removing the first CO_2 molecule, surrounded by adsorbed neighbouring CO_2 molecules, is energetically more favourable (corresponding to peak A1) as it eliminates repulsion. Further removal of the remaining CO_2 molecules requires more energy for desorption (corresponding to peaks A2–A4). In other words, we hypothesise that multiple oxidation peaks appear in this MOF because of numerous and distinct adsorption states, where CO_2 binding is affected by its surroundings. Notably, this study's peak separation (particularly between A1

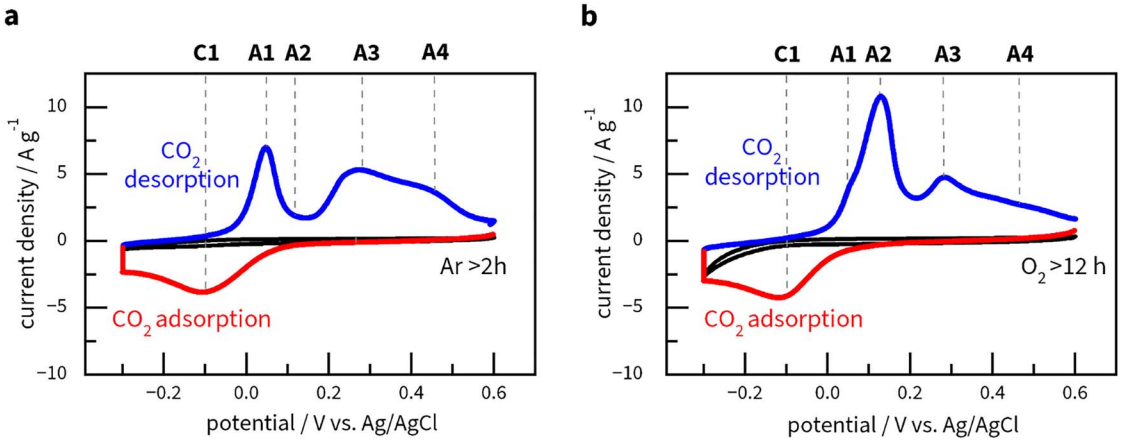

Fig. 4 CV curves recorded at $v = 10$ mV s^{-1} for the $Cu_3(HHTP)_2$-modified GC electrode: (a) black line – in an Ar-saturated electrolyte after stabilisation by cycling over two hours, red line – scan in the negative direction in a CO_2-saturated electrolyte, blue line – scan in the positive direction in a CO_2-saturated electrolyte, polarised for 10 min at −0.3 V. The C1-A1 peak separation is 150 mV. A CO_2 capacity of 2 mmol g^{-1} was obtained for the material by considering the area under the blue line in the anodic region (2.3 V A g^{-1}) and subsequently subtracting the area under CV in Ar (0.007 A V g^{-1}); $C = (A_{CO2} - A_{Ar})(v \times F)^{-1} = (2.3 - 0.007) \times (0.01 \times 96\,485)^{-1} = 2.38$ mmol g^{-1} (where C is the CO_2 capacity of the MOF, A_{CO2} is the area under the positive-going scan measured in CO_2, A_{Ar} is the area under the positive-going scan measured in Ar, v is the scan rate, and F is the Faraday constant). CO_2 capture capacity was estimated under the assumption that one electron induces adsorption–desorption of one CO_2 molecule.; (b) black line – scan in an O_2-saturated electrolyte after 5000 cycles (over 12 hours), red line – subsequent scan in a CO_2-saturated electrolyte in the negative direction, blue line – subsequent scan in a CO_2-saturated electrolyte in the positive direction, polarised for 10 min at −0.3 V. The C1–A2 peak separation is 240 mV.

and C1) is considerably smaller than those reported for other electrosorbents,[24,40,70] likely due to weaker CO_2 chemisorption.

To further validate the reversible CO_2 electrosorption performance beyond the standard three-electrode cell, we used an extended electrochemical flow battery setup with an electrode area of 9 cm^2 (Fig. S11a–c). In this system, $Cu_3(HHTP)_2$ was utilised to capture CO_2 directly from an airflow. While monitoring the system with a spectroscopic sensor, a distinct decrease in the CO_2 concentration was observed at negative potentials, indicating CO_2 capture (Fig. S11d). Upon switching to positive potentials, the CO_2 concentration increased, confirming the release process.

Altogether, CV, GCD, and DEMS measurements demonstrate that the redox behaviour of $Cu_3(HHTP)_2$ in a CO_2-saturated electrolyte is directly associated with CO_2 electrosorption. This finding highlights the potential of similar redox-active MOFs in the research, understanding, optimisation, and application of CO_2 electrosorption for carbon capture.

CO_2 electrosorption: distinction from anthraquinones

A previously known electrosorption mechanism involves the electrochemical reduction of an adsorption site, which alters its Lewis basicity, enabling CO_2 chemisorption.[71] Electrochemical reduction is usually denoted as step 'E', while chemisorption is denoted as step 'C'.[39] These two steps can occur in a concerted and sequential manner. For example, electrosorption on anthraquinones is thought to follow an 'ECEC' two-electron process, where two ketone moieties are reduced to alkoxide groups that bind two CO_2 molecules.[72] Reversing this process requires additional energy to break the formed bonds, resulting in a positive shift and separation of the anodic peaks. The data from DFT calculations reported in the literature supports this mechanism by linking binding energies to potential shifts.[40,41]

The MOF's resonance structure and +2 oxidation number of Cu imply that half of the O atoms in $HHTP^{3-}$ are alkoxides, while the other half are ketones. Thus, if a fully symmetric arrangement is assumed, the ratio between Cu atoms and ketones in the CuO_4 moiety equals 2. At first glance, the reduction of ketones could resemble the behaviour in anthraquinone, where CO_2 electrosorption follows a two-electron 'ECEC' process. Literature X-ray photoelectron spectroscopic data on $Cu_3(HHTP)_2$ suggest that Cu^{2+} and $HHTP^{3-}$ are partially reduced. Our CV data for $Cu_3(HHTP)_2$ in Ar- and CO_2-saturated electrolytes show a clear distinction from the features of (poly) anthraquinone.[39] The reduction curves in Fig. 3 and 4 show a singular reduction peak (C1), which the following mechanism can explain: when a CO_2 molecule binds to the MOF, it withdraws the electron density from the one-electron-reduced $Cu_3(HHTP)_2$. In a way, CO_2 reoxidises the MOF, which allows for its repeated reduction at C1, giving way to the adsorption of another CO_2 molecule until all four O sites in the CuO_4 moiety get occupied. Accordingly, as discussed above, the CV curve's oxidation side shows several peaks, indicating sequential desorption.

CO_2 electrosorption: new mechanism

Using DFT calculations, we further elucidated the mechanism of CO_2 adsorption on $Cu_3(HHTP)_2$, which should be regarded as a qualitative guide along with experimental charge–discharge measurements (Fig. S6) providing the quantitative assessment of energy consumption. DFT results revealed that CO_2 binds exclusively to the oxygen sites when the MOF is reduced by one

electron per Cu atom (Fig. S4). In this reduced state, the charge is evenly distributed between the CuO_4 moiety and the aromatic HHTP ligand (Fig. 5b). Copper gains approximately 0.1 electrons, maintaining its +2-oxidation state. In contrast, the HHTP ligands gain most of the added charge from the electron. This one-electron transfer resembles capacitive charging as in graphitic materials, along with partial contribution from the classical Cu^{2+}/Cu^{+} reduction. Such DFT-based insight aligns with the observed capacitive charging from Fig. 3a and S5.

Upon adsorption, the CO_2 molecule withdraws 0.5 electrons from the nearest Cu atom, effectively integrating itself into the MOF structure without significantly altering the charge distribution in the HHTP ligands. The potential energy of adsorption of gaseous CO_2 onto the hydrated surface is -6 kJ mol^{-1} (Fig. 5c). The lower absolute adsorption energy implies a lower cost for reversing the reaction. Recalculation into enthalpy gives an absolute value of -20 kJ mol^{-1}, which is notably lower when compared to other chemisorption mechanisms (Fig. 1 and Table S1).

DFT calculations and CV measurements show that CO_2 electrosorption on MOFs ($Cu_3(HHTP)_2$ in particular) differs from previously studied electrosorbents, such as anthraquinones.[39] First and foremost, pure $Cu_3(HHTP)_2$ does not show reduction–oxidation peaks. Second, DFT calculations reveal partial charge transfer to CO_2 during adsorption. Accounting for the latter, we can reevaluate the value of CO_2 capacity from 2 to 4 mmol g^{-1}, around $\frac{1}{4}$ of the theoretical maximum of 14.5 mmol g^{-1}. As mentioned above, due to the steric hindrance caused by the stacked layers of the MOF structure, not all oxygen sites may be accessible (Fig. 2 and 5). Likewise, a CO_2 adsorption event on one of the O sites in a CuO_4 moiety could hinder the adsorption of subsequent CO_2 molecules on the neighbouring O site within the same pore. That might limit the practical CO_2 capacity to around $\frac{1}{4}$ of the theoretical maximum of 14.5 mmol g^{-1}. Such estimation agrees with the highest experimentally obtained CO_2 capacity of 2–4 mmol g^{-1} (Fig. 4a). The sterical explanation also concurs with the work of Le *et al.*, where sterically hindered phenazine macrocycles exhibit twice lower capacity (per electron) than molecular phenazine.[73]

CO_2 electrosorption: future work

The DFT results highlight the essential role of copper in facilitating reversible CO_2 capture. Copper is a donor of electron density that the CO_2 molecule can withdraw upon adsorption. Thus, these results point to future strategies to further enhance the capacity and efficiency of MOFs under realistic conditions. Such methods include: (1) selecting metals with redox

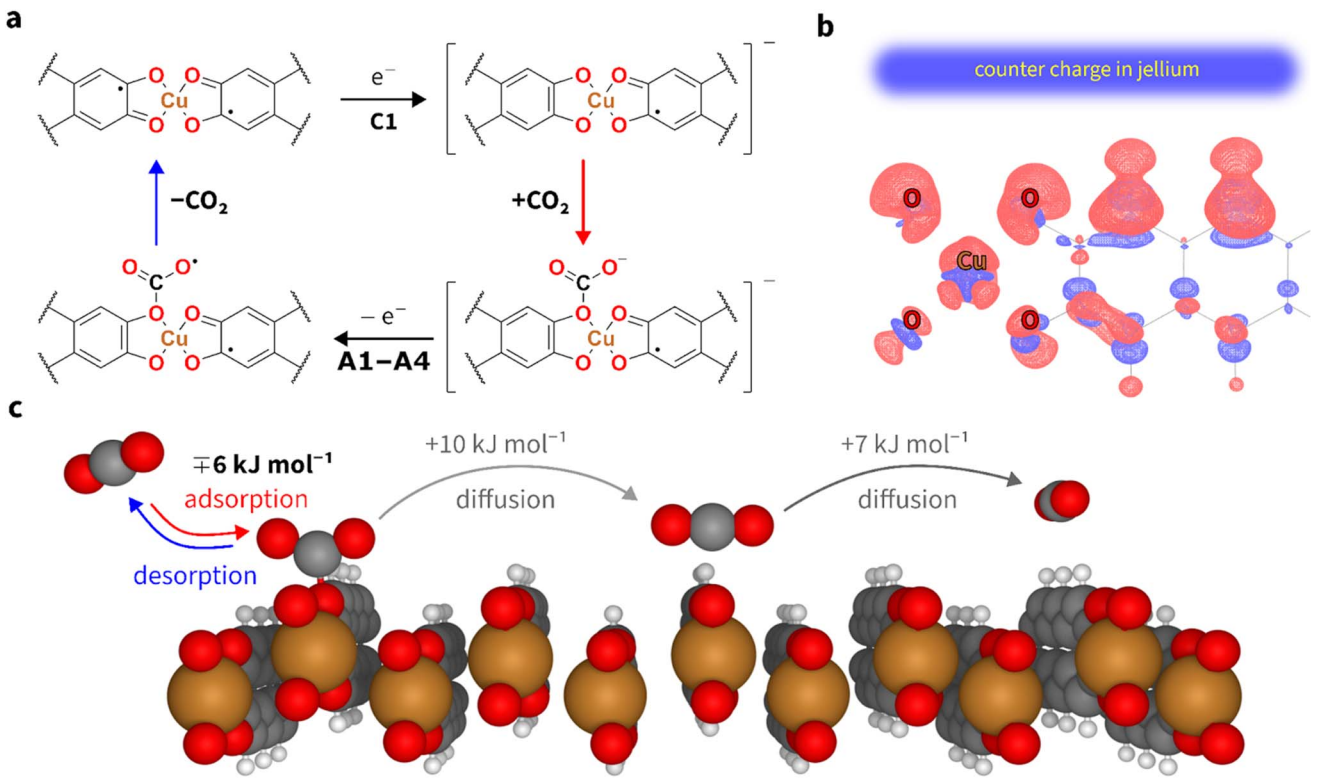

Fig. 5 (a) Possible 'EC'-type mechanism of CO_2 electrosorption in $Cu_3(HHTP)_2$. A localised model of the MOF shows just one of many resonance structures with localised single- and double-bonds; (b) isosurfaces of +0.002*e* (red) and −0.002*e* (blue) for charge density difference after adding 1*e* per Cu atom to a neutral 2D model of the MOF (see Fig. S2). It shows an almost homogeneous distribution of the extra electron over the CuO_4 moiety and aromatic ring. The counter-charge was located in the 0.3 nm wide jellium region 0.6 nm above Cu atom; (c) two-dimensional model of charged $Cu_3(HHTP)_2$ with CO_2 chemisorbed on the O site and physisorbed over Cu and aromatic rings. Numerical values represent potential adsorption and diffusion energies obtained from DFT calculations. The DFT analysis is based on a simplified 2D MOF model and is intended as a qualitative guide; quantitative energy consumption is provided by experimental charge–discharge data (Fig. S6).

properties that support reversible reduction, as copper does with its Cu^{2+}/Cu^{+} states (Fig. 3); (2) choosing adsorption sites with suitable Lewis basicity, such as chalcogenides and pnictogens; and (3) optimising the aromatic counterparts to enhance both stability and porosity, thereby increasing capacity and improving mass transport. Beyond this fundamental understanding, we also addressed more practical questions presented below.

$Cu_3(HHTP)_2$ stability

$Cu_3(HHTP)_2$ has been previously demonstrated to exhibit high structural and functional stability under demanding conditions. Eagleton *et al.* reported that $Cu_3(HHTP)_2$ coatings deposited on flexible textile and paper substrates retained their crystalline structure, strong interfacial adhesion, and functional performance even after exposure to mechanical abrasion and detergent washing.[80] These observations indicate the notable robustness and chemical persistence of the $Cu_3(HHTP)_2$ framework. Building on this established stability, we evaluated the behaviour of $Cu_3(HHTP)_2$ for CO_2 electrosorption using long-term CV experiments. In the range of −0.3 V to +0.7 V, the material demonstrates stability over 5000 cycles (Fig. S12). Copper underpotential deposition (Cu-UPD) tests (Fig. S13) confirm the absence of copper ions in the electrolyte after 1000 cycles. The actual degradation of $Cu_3(HHTP)_2$ happens below −0.4 V (Fig. S13). These findings suggest that $Cu_3(HHTP)_2$ remains stable and retains its CO_2 electrosorption capability over 24 h of CO_2 capture–release cycling.

$M_3(HHTP)_2$ MOFs with different metals

Among the studied MOFs, only $Cu_3(HHTP)_2$ could electrosorb CO_2 within the potential range stable for aqueous solutions. When exposed to CO_2, neither $Ni_3(HHTP)_2$ nor $Co_3(HHTP)_2$ showed any signs of CO_2 adsorption in CV measurements (Fig. S16). These observations suggest that the copper centres in $Cu_3(HHTP)_2$ are involved in the electrosorption mechanism. Accordingly, we hypothesise that the metal's reduction potential should be in the optimal potential range for CO_2 electrosorption to serve as an electron donor to the adsorbing CO_2 molecule. This makes the CuO_4 moiety in $Cu_3(HHTP)_2$ unique and emphasises the need to explore similar MOFs with various tunable geometric and electronic features. For example, CoPc–CuO_4 and NiPc–CuO_4 also show the ability to electrosorb CO_2,[74] and suggest that among the conductive MOFs, there could be those with adsorption energy above −15 kJ mol^{-1} and capacity over 5 mmol g^{-1}, *i.e.* in the desired region in Fig. 1a.

Methods

Synthesis of $Cu_3(HHTP)_2$

$Cu_3(HHTP)_2$ was synthesised using a literature procedure.[53] A solution of $Cu(NO_3)_2 \times 3H_2O$ (0.064 g, 0.265 mmol, 1.7 eq.) and 28% aqueous ammonia (1.1 mL, 7.71 mmol, 50 eq.) was prepared by dissolving them in Milli-Q water (1 mL). A dispersion of 2,3,6,7,10,11-hexahydroxytriphenylene (HHTP) was made separately by adding HHTP (0.051 g, 0.156 mmol, 1 eq.) to Milli-Q water (4.1 mL). The copper solution was added dropwise to the HHTP dispersion in a 20 mL vial, and the reaction mixture was heated at 80 °C for 24 hours. The resulting product was collected by centrifugation, washed with water, ethanol, and acetone, and dried at 80 °C for 24 hours, giving black particles of $Cu_3(HHTP)_2$ (0.049 g, 75%). The resulting $Cu_3(HHTP)_2$ material was characterised using scanning electron microscopy (SEM), energy dispersive X-ray spectroscopy (EDX), and powder X-ray diffraction (PXRD).

Physical characterisation

The $Cu_3(HHTP)_2$ MOF powder was secured onto stainless-steel scanning electron microscopy (SEM) stubs using adhesive high-purity carbon tabs. SEM images of the sample were obtained using a Tescan MIRA3 FEG-SEM, a high-performance field emission scanning electron microscope coupled with an Oxford Instruments X-maxN 80 energy dispersive X-ray spectroscopy (EDS) system for EDS acquisition and analysis. Imaging was conducted with a beam voltage of 5 kV with an In-Beam SE detector.

Powder X-ray diffraction (PXRD) data were collected over a 2θ range of 3–50° with a 0.050° step size under ambient conditions using a Bruker D8 Advance diffractometer with a LynxEye EX position sensitive detector. A homogeneous sample was packed and flattened on a steel sample holder, 8.5 mm in height, with a sample reception Ø of 25 mm. Computational structures used to produce the simulated PXRD patterns are available in ref. 75.

N_2 adsorption isotherms were recorded at 77 K using an Anton Paar Autosorb iQ-XR instrument. Gas sorption analysis was performed for six samples. Prior to adsorption measurements, the samples were activated by heating under vacuum at 110 °C for 16 hours to remove residual atmospheric CO_2 and H_2O from surfaces.

Electrochemical characterisation

A glassy carbon (GC) working electrode (Origalys) with an area of 0.196 cm^2 was modified with a layer of $Cu_3(HHTP)_2$ suspension. The MOF powder was dispersed in a 0.5% solution of Nafion in isopropanol, prepared by adding 5% Nafion (10 μL) to isopropanol (90 μL). $Cu_3(HHTP)_2$ (1 mg) was added to 1 mL of 0.5% Nafion solution in isopropanol, and the suspension was sonicated (NE00922, 40 kHz, 120 W) for 15 seconds. The suspension (5 μL) was dropcast to the surface of the electrode and subsequently dried in ambient air. The second layer was applied right after drying. The final $Cu_3(HHTP)_2$ loading on the electrode was 0.01 mg or 0.05 mg cm^{-2}.

A five-inlet electrochemical glass cell was used for CV, EIS and GCD experiments. CV measurements were performed in a three-electrode setup consisting of a GC working disk electrode (or Pt disk electrode, diameter 5 mm, Origalys), an Ag/AgCl (saturated KCl) reference electrode (or Pt wire electrode for EIS), and a GC rod counter electrode separated by a glass frit membrane in a five-inlet electrochemical cell. The electrolyte was 0.1 M sodium perchlorate ($NaClO_4$) solution prepared in Milli-Q water. CV scans were recorded at a sweep rate of 10 mV s^{-1}, typically in the potential ranges of −0.3 V to +0.6 V and

−0.8 V to +0.8 V *vs.* Ag/AgCl, unless otherwise noted. The cell was saturated with pure Ar, CO_2, O_2 or air, and during the experiments, a continuous flow of corresponding gas was maintained above the solution to prevent contamination. All CV curves were recorded by a Multi Autolab M204 potentiostat controlled by the Nova v2.1 software of Metrohm. Experiments were reproduced at least three times.

CO_2 gas flow cell measurements

Experiments were conducted in a flow electrochemical cell supplied with ambient air at the inlet. Two carbon paper (CP) electrodes, each with an area of 9 cm^2, were employed; the working electrode was coated by drop-casting 10 mg of Cu_3(-HHTP)$_2$ dispersed in 1 mL of 100% isopropanol, while the counter CP electrode was left unmodified (no Nafion or other ionomer binder was used in the electrode preparation). The electrodes were separated by a polyethersulfone membrane (Labbox MFPE-247-200). The outlet stream was monitored with an inline spectroscopic sensor Gas Lab GC018 to track CO_2 concentration. For adsorption, a potential of −0.3 V was applied for 300 s to saturate the working electrode with CO_2, followed by desorption at +0.5 V for 300 s.

Differential electrochemical mass spectrometry measurements

During electrochemical measurements, DEMS was employed for *in situ* monitoring of the adsorption and desorption of CO_2 on $Cu_3(HHTP)_2$. A Pfeiffer Prisma QMS 200 mass spectrometer equipped with a quadrupole detector and a secondary electron multiplier was coupled to a conventional three-electrode cell. A glassy carbon disk with a small cavity, approximately 1.5 mm in diameter, was used as the working electrode. The electrode was modified with a MOF suspension prepared by dispersing 5 mg of $Cu_3(HHTP)_2$ in 100 μL of isopropanol without the addition of Nafion, followed by sonication for 2 min. The resulting suspension was drop-cast onto the surface of the electrode and allowed to dry prior to electrochemical measurements. A PTFE membrane (Gore-Tex) was positioned within this cavity, allowing the simultaneous acquisition of mass spectrometric and cyclic voltammograms with optimal sensitivity. The experiments were conducted at a scan rate of 1 mV s^{-1} in a hanging meniscus configuration. The ion current for m/z = +44 [CO_2^+] was tracked during potential sweeps between +0.6 V and −0.4 V. Experiments were reproduced at least three times.

Density functional theory calculations

Density Functional Theory (DFT) calculations were performed using the Atomic Simulation Environment (ASE) version 3.23.0 (ref. 76) and the GPAW package version 24.1.0 (ref. 77) to model CO_2 adsorption on $Cu_3(HHTP)_2$. The RPBE exchange–correlation functional,[78] with D4 dispersion correction,[79] was employed alongside a projector augmented-wave method to describe core and valence electrons. Spin-polarisation was turned on, and the magnetic moment of ±1 was preset on Cu^{2+} ions, with alternating signs for distinct layers. The Brillouin zone was sampled with four k-points in the MOF plane and two k-points in perpendicular directions. CO_2 adsorption was modelled in finite-difference mode using a solvated jellium model,[60] with a constant counter charge of +1e per Cu atom positioned above the MOF surface. An implicit water layer was included to simulate solvation effects. Adsorption energies were calculated for three sites (above Cu atoms, O atoms, and aromatic rings) with optimisation of atomic positions until the residual forces were below 0.1 eV $Å^{-1}$. Enthalpy, entropy, and free energy values were evaluated at ideal gas and harmonic approximations through a vibrational analysis implemented in the ASE thermochemistry module.

Conclusions

This study demonstrated that conductive and redox-active metal–organic frameworks (MOFs) can reversibly electrosorb CO_2 under mild conditions. $Cu_3(HHTP)_2$, in particular, operates efficiently in aqueous solution at ambient temperature and in the presence of oxygen. This represents a significant advancement in CO_2 capture technology, as the studied class of materials – conductive and redox-active MOFs – can operate under the conditions required for direct air capture. However, to assess its practical application, a thorough technoeconomic and stability analysis is required. Our findings reveal that the mechanism of electrosorption in $Cu_3(HHTP)_2$ involves a synergistic interplay between copper centres, oxygen sites, and aromatic ligands. The redox activity of copper centres modulates the affinity at oxygen sites, enabling controlled adsorption and desorption cycles without the electrochemical reduction of CO_2. This mechanism is distinct from previous electrosorbents, such as polyanthraquinone, in which the process does not involve metal centres.

Based on the modelled mechanism, this study suggests optimising variable metal centres, adsorption sites, and aromatic structures to design new conductive redox-active MOFs capable of reversible CO_2 electrosorption. This represents a conceptual shift in CO_2 capture strategies, moving towards integrating conductive MOFs with specific redox and adsorption functionalities. Optimising the parameters identified in this study could lead to the development of the first generation of electrolytic cells for direct air capture of CO_2, ultimately reducing atmospheric CO_2 levels.

Author contributions

N. K., V. I., and V. G. conceived the project, designed the experiments and supervised the work. I. V. carried out electrochemical measurements. I. V. collected and interpreted the electrochemical data. N. Z. and A. K. synthesised the materials. K. A. M., A. C. F., and J. W. G. provided preliminary samples, while V. I., R. C., and V. K. performed the DFT calculations. T. T., H. Q., and P. C. ran physicochemical analyses. V. G., E. H., R. R., and J. S.-G. provided DEMS analysis. A. F., E. H., R. R., K. M. and J. S.-G. refined the manuscript. V. I., I. V., N. K., V. G., and N. Z. co-wrote the manuscript.

Conflicts of interest

There are no conflicts to declare.

Data availability

The data supporting the findings of this study are available within the article and its supplementary information (SI) files. The computational simulation data are available as an ASE database from Zenodo at https://doi.org/10.5281/zenodo.14216403. Any other data supporting this study's findings are available from the corresponding author upon reasonable request. Supplementary information is available. See DOI: https://doi.org/10.1039/d5ta08870d.

Acknowledgements

This work was supported by the Estonian Ministry of Education and Research (TK210), the Estonian Research Council (PRG3174, STP52 MOB3JD1208, PUTJD1245, PUTJD1244 and PRG1509), The State Shared Service Centre Astra+ Grant (2021-2027.1.01.25-1076), Ministerio de Ciencia, Innovación y Universidades (PID2022-137350NB-I00 and PID2022-138491OB-C32 (MCIN/AEI/10.13039/501100011033/FEDER, UE)), and the European Cooperation in Science and Technology Innovation Grant (COST CIG 18234, NanoCatML). Computational results were obtained using the UT Rocket High-Performance Computing Center of the University of Tartu.

References

1 M. Ozkan, A. B. Narappa, T. Namboodiri, Y. Chai, M. Babu, J. S. E. Jennings, Y. Gao, S. Tasneem, J. Lam, K. R. Talluri, R. Shang, C. S. Ozkan and J. M. Watkins, *iScience*, 2024, **27**, 109154.
2 S. Wynes, S. J. Davis, M. Dickau, S. Ly, E. Maibach, J. Rogelj, K. Zickfeld and H. D. Matthews, *Commun. Earth Environ.*, 2024, **5**, 498.
3 K. Shi, B. Guan, Z. Zhuang, J. Chen, Y. Chen, Z. Ma, C. Zhu, X. Hu, S. Zhao, H. Dang, J. Guo, L. Chen, K. Shu, Y. Li, Z. Guo, C. Yi, J. Hu and Z. Huang, *Energy Fuels*, 2024, **38**, 7665–7692.
4 M. Ozkan, *MRS Energy Sustainability*, 2025, **12**, 46–61.
5 M. S. Sorayani Bafqi, N. Aliyeva, H. Baskan-Bayrak, S. Dogan and B. Saner Okan, *Nano Futures*, 2024, **8**, 022002.
6 P. Wang, A. J. Robinson and S. Papadokonstantakis, *Front. Energy Res.*, 2024, **12**, 1412770.
7 O. A. Yafiee, F. Mumtaz, P. Kumari, G. N. Karanikolos, A. Decarlis and L. F. Dumée, *Chem. Eng. J.*, 2024, **497**, 154421.
8 C. Yi, B. Guan, Z. Zhuang, J. Chen, J. Guo, Y. Chen, Z. Ma, C. Zhu, S. Zhao, H. Dang, L. Chen, K. Shu, Y. Li, K. Shi, Z. Guo, J. Hu, X. Hu and Z. Huang, *Ind. Eng. Chem. Res.*, 2024, **63**, 11725–11758.
9 S. Zhang, Y. Shen, C. Zheng, Q. Xu, Y. Sun, M. Huang, L. Li, X. Yang, H. Zhou, H. Ma, Z. Li, Y. Zhang, W. Liu and X. Gao, *Front. Environ. Sci. Eng.*, 2024, **18**, 75.
10 Y. Hu, R. Gani, K. Sundmacher and T. Zhou, *Chem. Eng. Sci.*, 2024, **298**, 120423.
11 X. Y. D. Soo, J. J. C. Lee, W.-Y. Wu, L. Tao, C. Wang, Q. Zhu and J. Bu, *J. CO_2 Util.*, 2024, **81**, 102727.
12 X. An, P. Wang, X. Ma, X. Du, X. Hao, Z. Yang and G. Guan, *Carbon Resour. Convers.*, 2023, **6**, 85–97.
13 J. Hack, N. Maeda and D. M. Meier, *ACS Omega*, 2022, **7**, 39520–39530.
14 X. Y. D. Soo, J. J. C. Lee, W.-Y. Wu, L. Tao, C. Wang, Q. Zhu and J. Bu, *J. CO_2 Util.*, 2024, **81**, 102727.
15 L. Küng, S. Aeschlimann, C. Charalambous, F. McIlwaine, J. Young, N. Shannon, K. Strassel, C. N. Maesano, R. Kahsar, D. Pike, M. Van Der Spek and S. Garcia, *Energy Environ. Sci.*, 2023, **16**, 4280–4304.
16 K. N. Jayarapu, A. Mathur, X. Li, A. Liu, L. Zhang, J. Kim, H. Kim, S. K. Kuk and Y. Liu, *Adv. Funct. Mater.*, 2024, 2402355.
17 K. Sun, M. Tebyetekerwa, H. Zhang, X. Zeng, Z. Wang, Z. Xu, T. E. Rufford and X. Zhang, *Adv. Energy Mater.*, 2024, **14**, 2400625.
18 S. R. Wenger and D. M. D'Alessandro, *ACS Sustain. Chem. Eng.*, 2024, **12**, 4789–4794.
19 S. P. Teong and Y. Zhang, *Green Energy Environ.*, 2024, **9**, 413–416.
20 E. Wang, R. Navik, Y. Miao, Q. Gao, D. Izikowitz, L. Chen and J. Li, *Cell Rep. Phys. Sci.*, 2024, **5**, 101791.
21 G. Liu, A. Yang and R. C. Darton, *ACS Sustain. Chem. Eng.*, 2024, **12**, 3951–3965.
22 H. Seo, M. P. Nitzsche and T. A. Hatton, *Acc. Chem. Res.*, 2023, **56**, 3153–3164.
23 Y. Hu, R. Gani, K. Sundmacher and T. Zhou, *Chem. Eng. Sci.*, 2024, **298**, 120423.
24 S. Voskian and T. A. Hatton, *Energy Environ. Sci.*, 2019, **12**, 3530–3547.
25 M. Burunova, I. Vetik, A. Stepanova, K. Kudelina, N. Kongi and V. Ivaništšev, *ChemrXiv*, 2026, preprint, DOI: 10.26434/chemrxiv-2026-g3z.
26 Y. Hu, X. Li, J. Liu, L. Li and L. Zhang, *Greenhouse Gases:Sci. Technol.*, 2018, **8**, 713–720.
27 V. Hiremath, A. H. Jadhav, H. Lee, S. Kwon and J. G. Seo, *Chem. Eng. J.*, 2016, **287**, 602–617.
28 J. Kumełan, Á. Pérez-Salado Kamps, D. Tuma and G. Maurer, *J. Chem. Thermodyn.*, 2006, **38**, 1396–1401.
29 O. J. García-Ricard and A. J. Hernández-Maldonado, *J. Phys. Chem. C*, 2010, **114**, 1827–1834.
30 S. Karka, S. Kodukula, S. V. Nandury and U. Pal, *ACS Omega*, 2019, **4**, 16441–16449.
31 J. W. Lee, H. Ahn, S. Kim and Y. T. Kang, *J. Cleaner Prod.*, 2023, **390**, 136141.
32 M. Minelli, E. Papa, V. Medri, F. Miccio, P. Benito, F. Doghieri and E. Landi, *Chem. Eng. J.*, 2018, **341**, 505–515.
33 F. Su, C. Lu, S.-C. Kuo and W. Zeng, *Energy Fuels*, 2010, **24**, 1441–1448.
34 M. E. Zick, S. M. Pugh, J.-H. Lee, A. C. Forse and P. J. Milner, *Angew. Chem., Int. Ed.*, 2022, **61**, e202206718.
35 National Academies of Sciences, Engineering, and Medicine, *Negative Emissions Technologies and Reliable Sequestration: A Research Agenda*, 2019, The National Academies Press,

Washington, DC, https://www.nationalacademies.org/projects/DELS-BASCPR-16-01/publication/25259.
36 A. M. Zito, L. E. Clarke, J. M. Barlow, D. Bím, Z. Zhang, K. M. Ripley, C. J. Li, A. Kummeth, M. E. Leonard, A. N. Alexandrova, F. R. Brushett and J. Y. Yang, *Chem. Rev.*, 2023, **123**, 8069–8098.
37 Y. Guo, M. Massen-Hane, G. Endy and T. A. Hatton, *Adv. Mater.*, 2024, **36**, 2407567.
38 J. Liu, M. Yang, X. Zhou and Z. Meng, *J. Am. Chem. Soc.*, 2024, **146**(48), 33093–33103.
39 F. Simeon, M. C. Stern, K. M. Diederichsen, Y. Liu, H. J. Herzog and T. A. Hatton, *J. Phys. Chem. C*, 2022, **126**, 1389–1399.
40 X. Li, X. Zhao, Y. Liu, T. A. Hatton and Y. Liu, *Nat. Energy*, 2022, **7**, 1065–1075.
41 A. T. Bui, N. A. Hartley, A. J. W. Thom and A. C. Forse, *J. Phys. Chem. C*, 2022, **126**, 14163–14172.
42 M. Ozkan, A. Shiner, N. Kongi, T. A. Hatton, S. Oldham and E. Sanders, *Chem*, 2024, **10**, 3–6.
43 J. E. Ellis, S. E. Crawford and K.-J. Kim, *Mater. Adv.*, 2021, **2**, 6169–6196.
44 O. Kocyigit, A. N. Kursunlu and E. Guler, *J. Hazard. Mater.*, 2010, **183**, 334–340.
45 M. Yao, X. Lv, Z. Fu, W. Li, W. Deng, G. Wu and G. Xu, *Angew. Chem., Int. Ed.*, 2017, **56**, 16510–16514.
46 B. Hoppe, K. D. J. Hindricks, D. P. Warwas, H. A. Schulze, A. Mohmeyer, T. J. Pinkvos, S. Zailskas, M. R. Krey, C. Belke, S. König, M. Fröba, R. J. Haug and P. Behrens, *CrystEngComm*, 2018, **20**, 6458–6471.
47 S. Gu, Z. Bai, S. Majumder, B. Huang and G. Chen, *J. Power Sources*, 2019, **429**, 22–29.
48 M. Yao, J. Xiu, Q. Huang, W. Li, W. Wu, A. Wu, L. Cao, W. Deng, G. Wang and G. Xu, *Angew. Chem., Int. Ed.*, 2019, **58**, 14915–14919.
49 M. Wang, R. Dong and X. Feng, *Chem. Soc. Rev.*, 2021, **50**, 2764–2793.
50 L. S. Xie, G. Skorupskii and M. Dincă, *Chem. Rev.*, 2020, **120**, 8536–8580.
51 K. W. Nam, S. S. Park, R. Dos Reis, V. P. Dravid, H. Kim, C. A. Mirkin and J. F. Stoddart, *Nat. Commun.*, 2019, **10**, 4948.
52 M. Hmadeh, Z. Lu, Z. Liu, F. Gándara, H. Furukawa, S. Wan, V. Augustyn, R. Chang, L. Liao, F. Zhou, E. Perre, V. Ozolins, K. Suenaga, X. Duan, B. Dunn, Y. Yamamto, O. Terasaki and O. M. Yaghi, *Chem. Mater.*, 2012, **24**, 3511–3513.
53 J. W. Gittins, C. J. Balhatchet, S. M. Fairclough and A. C. Forse, *Chem. Sci.*, 2022, **13**, 9210–9219.
54 R. W. Day, D. K. Bediako, M. Rezaee, L. R. Parent, G. Skorupskii, M. Q. Arguilla, C. H. Hendon, I. Stassen, N. C. Gianneschi, P. Kim and M. Dincă, *ACS Cent. Sci.*, 2019, **5**, 1959–1964.
55 W. Li, K. Ding, H. Tian, M. Yao, B. Nath, W. Deng, Y. Wang and G. Xu, *Adv. Funct. Mater.*, 2017, **27**, 1702067.
56 V. Rubio-Giménez, M. Galbiati, J. Castells-Gil, N. Almora-Barrios, J. Navarro-Sánchez, G. Escorcia-Ariza, M. Mattera, T. Arnold, J. Rawle, S. Tatay, E. Coronado and C. Martí-Gastaldo, *Adv. Mater.*, 2018, **30**, 1704291.
57 S. Gu, Z. Bai, S. Majumder, B. Huang and G. Chen, *J. Power Sources*, 2019, **429**, 22–29.
58 Z. Zhang, D. S. Valente, Y. Shi, D. K. Limbu, M. R. Momeni and F. A. Shakib, *ACS Appl. Mater. Interfaces*, 2023, **15**, 9494–9507.
59 S.-J. Shin, J. W. Gittins, M. J. Golomb, A. C. Forse and A. Walsh, *J. Am. Chem. Soc.*, 2023, **145**, 14529–14538.
60 G. Kastlunger, P. Lindgren and A. A. Peterson, *J. Phys. Chem. C*, 2018, **122**, 12771–12781.
61 W. Zhao, T. Chen, W. Wang, S. Bi, M. Jiang, K. Y. Zhang, S. Liu, W. Huang and Q. Zhao, *Adv. Mater. Interfaces*, 2021, **8**, 2100308.
62 J. W. Gittins, C. J. Balhatchet, S. M. Fairclough and A. C. Forse, *Chem. Sci.*, 2022, **13**, 9210–9219.
63 F. Simeon, M. C. Stern, K. M. Diederichsen, Y. Liu, H. J. Herzog and T. A. Hatton, *J. Phys. Chem. C*, 2022, **126**, 1389–1399.
64 Y. Liu, H.-Z. Ye, K. M. Diederichsen, T. Van Voorhis and T. A. Hatton, *Nat. Commun.*, 2020, **11**, 2278.
65 N. A. Hartley, Z. Xu, T. Kress and A. C. Forse, *Mater. Today Energy*, 2024, **45**, 101689.
66 S. J. Ashton, in *Design, Construction and Research Application of a Differential Electrochemical Mass Spectrometer (DEMS)*, Springer Berlin Heidelberg, Berlin, Heidelberg, 2012, vol. 8, pp. 9–27.
67 G. Zhang, Y. Cui and A. Kucernak, *ACS Catal.*, 2022, **12**, 6180–6190.
68 H. Baltruschat, *J. Am. Soc. Mass Spectrom.*, 2004, **15**, 1693–1706.
69 D. B. Trimarco, S. B. Scott, A. H. Thilsted, J. Y. Pan, T. Pedersen, O. Hansen, I. Chorkendorff and P. C. K. Vesborg, *Electrochim. Acta*, 2018, **268**, 520–530.
70 G. Iijima, J. Naruse, H. Shingai, K. Usami, T. Kajino, H. Yoto, Y. Morimoto, R. Nakajima, T. Inomata and H. Masuda, *Energy Fuels*, 2023, **37**, 2164–2177.
71 S. E. Renfrew, D. E. Starr and P. Strasser, *ACS Catal.*, 2020, **10**, 13058–13074.
72 A. Hemmatifar, J. S. Kang, N. Ozbek, K. Tan and T. A. Hatton, *ChemSusChem*, 2022, **15**, e202102533.
73 P. H. Le, A. Liu, L. B. Zasada, J. Geary, A. A. Kamin, D. S. Rollins, H. A. Nguyen, A. M. Hill, Y. Liu and D. J. Xiao, *Angew. Chem., Int. Ed.*, 2024, e202421822.
74 Z. Meng, J. Luo, W. Li and K. A. Mirica, *J. Am. Chem. Soc.*, 2020, **142**, 21656–21669.
75 J. W. Gittins, C. J. Balhatchet, Y. Chen, C. Liu, D. G. Madden, S. Britto, M. J. Golomb, A. Walsh, D. Fairen-Jimenez, S. E. Dutton and A. C. Forse, *J. Mat. Chem. A*, 2021, **9**, 16006–16015.
76 A. H. Larsen, J. J. Mortensen, J. Blomqvist, I. E. Castelli, R. Christensen, M. Dulak, J. Friis, M. N. Groves, B. Hammer, C. Hargus, E. D. Hermes, P. C. Jennings, P. B. Jensen, J. Kermode, J. R. Kitchin, E. L. Kolsbjerg, J. Kubal, K. Kaasbjerg, S. Lysgaard, J. B. Maronsson, T. Maxson, T. Olsen, L. Pastewka, A. Peterson, C. Rostgaard, J. Schiøtz, O. Schütt, M. Strange, K. S. Thygesen, T. Vegge, L. Vilhelmsen, M. Walter, Z. Zeng

and K. W. Jacobsen, *J. Phys.: Condens. Matter*, 2017, **29**, 273002.

77 J. J. Mortensen, A. H. Larsen, M. Kuisma, A. V. Ivanov, A. Taghizadeh, A. Peterson, A. Haldar, A. O. Dohn, C. Schäfer, E. Ö. Jónsson, E. D. Hermes, F. A. Nilsson, G. Kastlunger, G. Levi, H. Jónsson, H. Häkkinen, J. Fojt, J. Kangsabanik, J. Sødequist, J. Lehtomäki, J. Heske, J. Enkovaara, K. T. Winther, M. Dulak, M. M. Melander, M. Ovesen, M. Louhivuori, M. Walter, M. Gjerding, O. Lopez-Acevedo, P. Erhart, R. Warmbier, R. Würdemann, S. Kaappa, S. Latini, T. M. Boland, T. Bligaard, T. Skovhus, T. Susi, T. Maxson, T. Rossi, X. Chen, Y. L. A. Schmerwitz, J. Schiøtz, T. Olsen, K. W. Jacobsen and K. S. Thygesen, *J. Chem. Phys.*, 2024, **160**, 092503.

78 B. Hammer, L. B. Hansen and J. K. Nørskov, *Phys. Rev. B: Condens. Matter Mater. Phys.*, 1999, **59**, 7413–7421.

79 E. Caldeweyher, J.-M. Mewes, S. Ehlert and S. Grimme, *Phys. Chem. Chem. Phys.*, 2020, **22**, 8499–8512.

80 A. M. Eagleton, M. Ko, R. M. Stolz, N. Vereshchuk, Z. Meng, L. Mendecki, A. M. Levenson, C. Huang, K. C. MacVeagh, A. Mahdavi-Shakib, J. J. Mahle, G. W. Peterson, B. G. Frederick and K. A. Mirica, *J. Am. Chem. Soc.*, 2022, **144**(51), 23297–23312.